(Received 18 July 2025, Accepted 15 September 2025, Scheduled 30 September 2025)

Synthesis of Miniaturized Frequency-Selective Surfaces Using Stepped Impedance Resonators for Spurious Shift Control

Salem Bousnadji[1], Larbi Talbi[1], Khelifa Hettak[1], and Mohamed Mamdouh M. Ali[2,*]

[1]*Department of Electrical and Computer Engineering, University of Quebec in Outaouais, Gatineau, QC, Canada*
[2]*Department of Electrical Engineering, Faculty of Engineering, Assiut University, Egypt*

ABSTRACT: Frequency-Selective Surfaces (FSSs) are structures designed to selectively transmit or reflect electromagnetic waves, making them essential for applications requiring precise control over frequency bands and wave propagation characteristics. However, traditional FSS designs face challenges such as fixed geometries, limited scalability, and poor bandwidth efficiency, often requiring compromises between size reduction and performance. To address these limitations, this work introduces the use of Stepped Impedance Resonators (SIRs) to synthesize miniaturized FSS structures with four-legged elements (FLEs). By combining transmission line theory, SIR equations, and parallel coplanar stripline models, an innovative synthesis method is proposed, enabling precise control over spurious frequencies and resulting in a 54% reduction in unit-cell size without sacrificing performance. This approach significantly enhances the feasibility of compact FSS applications. To further improve performance, an arrow-bending technique was introduced to reduce the coupling between adjacent cells, yielding a 30% improvement in isolation. Three distinct surface designs have been fabricated and tested under both normal incidence and oblique angles for TE and TM modes. These designs include the SIR-based FSS cell, an enhanced design featuring arrow bending, and a reverse arrow formation intended to reduce edge effects between adjacent cells. Additionally, measurements demonstrate excellent performance stability, with tolerance maintained for incident angles up to 60°. Experimental validation confirms effective blocking at 10 GHz and highlights the robustness of the design across varying incident angles. Prototypes fabricated from the miniaturized FSS elements show excellent agreement with simulations, underscoring the potential of this method for advanced applications in communications, radar, and electromagnetic shielding.

1. INTRODUCTION

Frequency Selective Surfaces (FSSs) play a pivotal role in modern electromagnetic applications, offering precise control over frequency bands for technologies like spatial filtering, communication systems, and radar design [1–3]. The frequency response of an FSS is primarily determined by the size, shape, and periodicity of its elements. Other factors that influence the frequency response include the thickness of elements, the dielectric permittivity of the substrate, the thickness of the metallic screen, and the direction of the incident wave [4–6].

A variety of element shapes have been explored in the design of FSSs [7]. Notable applications of FSSs include phase manipulation [8, 9], backscattering control [10, 11], antenna gain enhancement [12, 13], absorber [14], wearable devices [15], antenna radomes [16], electromagnetic shielding [17], and mobile and satellite communication systems [18]. Traditional FSS designs rely on mutual interactions between unit-cells to achieve the desired frequency response. As a result, a large number of unit-cells are required to observe the necessary frequency-selective behavior, leading to an electrically large surface. In some applications, however, such as those requiring low sensitivity to the angle of incidence or a uniform phase front, the screen size must be compact.

To overcome these challenges, a new class of FSSs, known as miniaturized-element frequency surfaces, has been developed [19, 20]. FSSs typically consist of resonance elements, and several techniques have been proposed to reduce their size while improving frequency performance. One approach involves high-impedance multilayered mushroom-type surfaces, which effectively reduce the unit-cell profile [7, 21]. Another method uses meander line schemes to create smaller surfaces [22]. Additionally, fractal elements have been suggested as a space-filling technique to further minimize element size [23]. A high-quality FSS element should maintain a stable resonant frequency across various angles of incidence and polarizations. Loop-type elements, such as three- and four-legged loaded elements, as well as simple circular and square loops, are well-known candidates for achieving this feature [19, 24]. To analyze periodic elements, an equivalent circuit model is often extracted, with parameters primarily derived from full-wave simulations [25]. With an accurate model, the desired frequency response such as center frequency, bandwidth, insertion loss, and tuning range can be synthesized using optimization methods in a relatively short time, offering a more efficient alternative to traditional numerical simulators [26].

The goal of this paper is to introduce a novel method for analyzing and designing frequency-selective surfaces. The synthesis of metasurfaces requires the precise control over electromagnetic properties, demanding advanced methodologies and

* Corresponding author: Mohamed Mamdouh M. Ali (mohamed.ali@ieee.org).

greater flexibility in design parameters. This work draws inspiration from the Stepped Impedance Resonator (SIR) technique, a method traditionally employed in spatial filter design to control frequency responses with high precision. While SIR methods have been extensively utilized in microwave and analog filter design, their application to FSSs remains underexplored [27, 28]. A notable prior study utilized SIR method in conjunction with an equivalent circuit model and full-wave simulations to develop a 3D spatial filter [29]. However, such designs often result in bulky configurations that are unsuitable for thin, single-layer metasurfaces. To address challenges such as angular stability, miniaturization, and suppression of spurious frequencies in compact metasurfaces, a rigorous and adaptable synthesis method is essential. To the best of our knowledge, this work presents the first systematic application of SIR synthesis to single-layer four-legged FSS elements, where closed-form SIR equations are combined with coplanar-strip parameter extraction to yield accurate initial unit-cell dimensions. This analytical starting point reduces the reliance on purely empirical optimization, which is reserved for fine tuning rather than complete geometry discovery.

Building on the limitations of conventional FSS designs, this work proposes a novel synthesis framework that leverages stepped impedance resonators to achieve significant miniaturization and enhanced control over spurious frequencies. Unlike traditional approaches, where the resonant frequency is critically dependent on the width and thickness of metallic traces, the proposed SIR-based FSSs decouple the resonant frequency from physical trace dimensions by utilizing the impedance ratio between adjacent segments as the primary determinant. This fundamental shift in design methodology introduces transformative advantages, including topological flexibility, where identical frequency responses can be achieved with varied geometries tailored to fabrication constraints and enhanced robustness against manufacturing variations such as etching inaccuracies or irregularities in inkjet printing. Furthermore, the independence of resonant frequency from trace thickness ensures a higher degree of tolerance during the fabrication process. In addition, the closed-form equations inherent to the SIR method provide precise initial estimations of resonant frequencies, significantly accelerating the design process compared to conventional empirical approaches. By integrating these advantages with advanced modeling techniques, such as transmission line theory and parallel coplanar stripline analysis, the proposed method achieves a 54% reduction in unit-cell size while maintaining optimal frequency performance. In this work, isolation is defined as the suppression of mutual coupling between adjacent FSS unit cells, which directly affects spurious resonance suppression and angular stability. The incorporation of an arrow-bending modification effectively enhances isolation, improving the inter-element transmission from approximately 18 dB in the baseline SIR-based design to 25 dB, corresponding to a 30% improvement at the design frequency. To validate this synthesis framework, three distinct configurations including SIR-based, arrow-bent, and reverse-arrow designs are fabricated and rigorously tested under both normal and oblique incidence for TE and TM modes. This integration of circuit-level synthesis with spatial-wave behavior has not been previously reported in single-layer FSS miniaturization studies. This innovative approach eliminates reliance on full-wave software optimization, ensuring angle stability up to 60° and robust performance at 10 GHz, thereby addressing the key limitations of conventional FSS designs and advancing the state of metasurface synthesis.

The rest of this paper is organized as follows. Section 2 focuses on the design and analysis of SIR-based unit cells, providing foundational principles of the approach. Section 3 explores the analysis of parallel co-planar strips as critical elements in FSS design. Section 4 details the synthesis of the FSS structure using SIR methodology. Section 5 presents the evolution of unit cell designs aimed at enhancing FSS performance. Section 6 provides experimental results validating the proposed designs, while Section 7 evaluates their performance through detailed comparisons. Finally, Section 8 concludes the work and outlines potential applications of the proposed methodology.

2. DESIGN AND ANALYSIS OF SIR-BASED UNIT CELLS

In frequency-selective surfaces design, the unit cell is fundamental in determining performance, particularly in terms of resonance frequency and frequency selectivity. Traditionally, unit cells are constructed using parallel conductive strips, as shown in Fig. 1(a). Using Rogers RT/Duroid 6002 as the substrate material, with a thickness of 0.76 mm, the resonance frequency of 10 GHz is achieved with specific physical parameters, namely $w = g = 0.2$ mm and period $L = \lambda_g/2 = 10.94$ mm, where λ_g is the guided wavelength at 10 GHz. When an incident wave interacts with the structure, an electrical current is induced on the parallel traces. However, in conventional designs, spurious frequencies are poorly suppressed, significantly limiting performance. Although these parameters meet fabrication constraints, addressing spurious frequencies remains a key challenge. To determine the structure's frequency characteristics without analyzing its equivalent circuit model, coupled lines theory can be used in combination with SIRs. Equivalent cir-

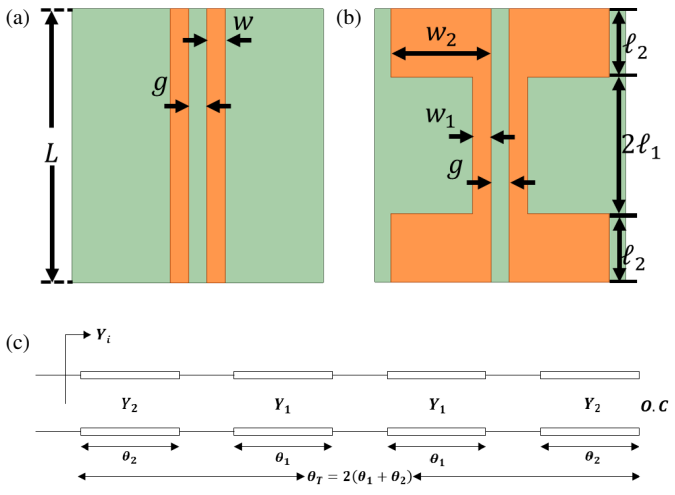

FIGURE 1. Unit-cell schematics: (a) Conventional unloaded element formation, (b) topology of stepped impedance resonator (SIR), and (c) transmission-line equivalent circuit.

cuits only provide qualitative analysis around the resonance frequency and do not fully capture the behavior of spurious frequencies.

To address the limitations of conventional designs, a novel unit-cell design based on stepped impedance resonators is introduced in Fig. 1(b). This configuration introduces alternating impedance sections to enhance frequency selectivity while reducing spurious responses. The SIR-based unit cell incorporates traces with distinct characteristic impedances, denoted as Z_{01} and Z_{02}, connected via a stepped geometry. This design exploits the principle that the impedance ratio $K = \frac{Z_{02}}{Z_{01}}$ governs the resonance and spurious frequencies of the structure. To provide an intuitive understanding of the SIR behavior, the equivalent transmission line (TL) circuit model is illustrated in Fig. 1(c). This model enables analytical evaluation of input admittance and impedance, providing a straightforward way to estimate the resonance and spurious frequencies without relying solely on full-wave simulations.

To simplify calculations, the assumption of equal electrical lengths ($\theta_0 = \theta_1 = \theta_2$) is made for all traces. This assumption reduces complexity and allows for more manageable expressions of the input admittance and impedance. The input admittance of the transmission line can be expressed as:

$$Y_{\text{in1}} = jY_2 \tan^2 \theta_2 \tag{1}$$

The characteristic impedances and their relationship to admittance are given as:

$$Z_{01} = \frac{1}{Y_1}, \quad Z_{02} = \frac{1}{Y_2}, \quad Z_{\text{in1}} = \frac{1}{jY_2 \tan^2 \theta_2} \tag{2}$$

The equivalent impedance and admittance of the structure become:

$$Z_i = Z_{01} \cdot \frac{Z_{\text{in1}} + jZ_{01} \tan \theta_1}{Z_{01} + jZ_{\text{in1}} \tan \theta_1} \tag{3}$$

$$Y_i = Y_1 \cdot \frac{Z_{01} + jZ_{\text{in1}} \tan \theta_1}{Z_{\text{in1}} + jZ_{01} \tan \theta_1} \tag{4}$$

Further simplification yields:

$$Y_i = jY_2 \cdot \frac{2(K \tan \theta_1 + \tan \theta_2)(K - \tan \theta_1 \tan \theta_2)}{K(1 - \tan^2 \theta_1)(1 - \tan^2 \theta_2) - 2(1 + K^2) \tan \theta_1 \tan \theta_2} \tag{5}$$

For the case $\theta_0 = \theta_1 = \theta_2$, the expression is simplified to:

$$Y_i = jY_2 \cdot \frac{2(K+1)(K - \tan^2 \theta_0) \tan \theta_0}{K(1 - 2\tan^2 \theta_0 + \tan^4 \theta_0) - 2(1 + K^2) \tan^2 \theta_0} \tag{6}$$

The resonance condition $Y_i = 0$ occurs when:

$$\tan \theta_1 \cdot \tan \theta_2 = K \tag{7}$$

As shown in Fig. 2(a), this condition defines the resonance frequency of the SIR line. The resonance can be tuned by adjusting the parameters of θ_2 and K, given the fixed electrical length $\theta_T = 2(\theta_1 + \theta_2)$, considering fabrication constraints [27]. This electrical length plays a key role in determining the resonance frequency and allows for better design optimization.

The analysis of spurious frequencies (θ_s) is crucial for improving the design's frequency selectivity. Spurious frequencies are identified by the condition:

$$\tan^2 \theta_0 = K \quad \text{and} \quad \theta_0 = \tan^{-1}(\sqrt{K}) \tag{8}$$

The first spurious frequency is:

$$\frac{f_{s1}}{f_0} = \frac{\pi}{2 \tan^{-1}(\sqrt{K})} \tag{9}$$

Subsequent spurious frequencies follow as:

$$\frac{f_{s2}}{f_0} = 2\left(\frac{f_{s1}}{f_0}\right) - 1 \tag{10}$$

$$\frac{f_{s3}}{f_0} = 2\left(\frac{f_{s1}}{f_0}\right) \tag{11}$$

This methodology illustrates how parameter K offers control over both resonance and spurious frequencies, enabling fine-tuning of the unit cell to meet specific design objectives. The variation of spurious frequencies with K, as shown in Fig. 2(b), enhances the design flexibility, allowing for optimized performance across various applications.

3. ANALYSIS OF PARALLEL CO-PLANAR STRIPS FOR FSS

The stepped impedance resonator technique leverages parallel co-planar strips (CPSs) to synthesize frequency-selective surfaces with a defined reference impedance, enabling precise control over electromagnetic properties. As shown in Fig. 3, the CPS structure consists of two parallel metallic strips of finite width (W), separated by inter-strip spacing (S). The substrate parameters include thickness (h), relative permittivity (ε_r), and conductor thickness (t) [30, 31]. Unlike traditional designs, the CPS configuration lacks a ground plane, making the calculation of characteristic impedance and permittivity challenging. Currently, no exact closed-form expressions are available to compute these parameters directly; accurate designs typically rely on numerical extraction or calibrated approximations [32, 33]. On the other hand, the two coupled lines provide a reference impedance that can be utilized for detailed circuit analysis through full-wave simulation tools. In this work, a systematic methodology has been developed leveraging a high-frequency electromagnetic field simulation software (Ansys HFSS) to evaluate the even and odd effective relative permittivity (ε_{effe} and ε_{effo}) under varying polarization conditions [34]. Additionally, a parametric approach was employed to account for the finite substrate thickness, enabling precise determination of the even and odd characteristic impedances (Z_{0e} and Z_{0o}). This refinement in modeling not only enhances the accuracy of the impedance and permittivity characterization

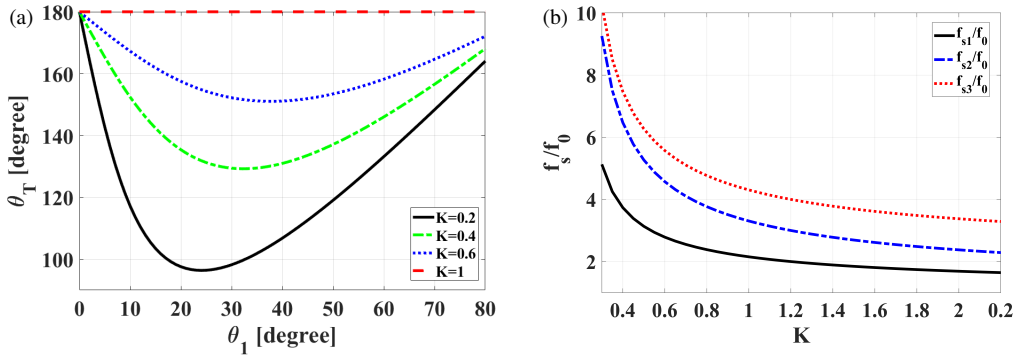

FIGURE 2. Effect of the K parameter on the SIR element: (a) Resonance frequency condition for various K, and (b) spurious resonance frequency analysis of the SIR-based unit cell using the analytical solution.

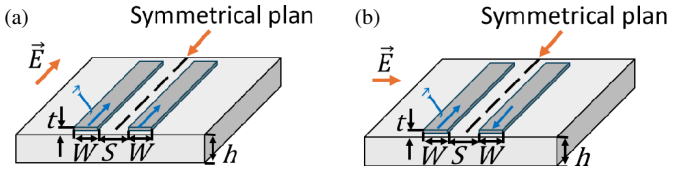

FIGURE 3. Co-planar strip structure current distribution: (a) Even mode, and (b) odd mode.

but also facilitates the optimized design of CPS structures for FSS applications.

The CPS structure supports both even and odd modes of propagation. In even mode, as illustrated in Fig. 3(a), the current on the two strips flows in the same direction, forming a symmetrical configuration. This can be approximated using an imaginary magnetic wall along the symmetry plane of the structure. Conversely, in odd mode, depicted in Fig. 3(b), the currents on the two strips flow in opposite directions, creating an anti-symmetrical configuration. An imaginary electrical wall is considered along the symmetry plane of the structure in this case. To evaluate the design's performance, parametric studies are conducted. For the even mode, variations in characteristic impedance and permittivity are examined by altering the trace width (W) and inter-strip spacing (S), as shown in Fig. 4. Similar studies are conducted for the odd mode, where the electric field distribution couples the CPS lines in the absence of a ground plane. Results, summarized in Fig. 5, reveal how changes in W and S affect the line impedance and permittivity. These parametric analyses are critical for finalizing geometrical dimensions of the frequency-selective surface. The obtained simulation charts guide the selection of W and S values for optimizing FSS performance.

4. SYNTHESIZING THE FSS STRUCTURE WITH SIR

Designing frequency selective surfaces often requires balancing theoretical objectives with practical constraints imposed by fabrication processes. The synthesis of an FSS aims to achieve desired electromagnetic characteristics while accommodating these constraints. Two key approaches have been proposed to guide this process: introducing flexibility in the synthesizing algorithm and enabling the design of unit cells with diverse topologies. The integration of the step-impedance resonator concept facilitates both approaches, particularly when dealing with dimensional restrictions, such as maintaining a 200 µm minimum gap between metallic surfaces.

To address these challenges, an algorithm has been developed to systematically derive solutions that satisfy both theoretical and practical requirements. The synthesis process begins by specifying the target resonance frequency and minimum spurious frequency, proceeding through three distinct steps:

1. Selecting W_1: Choose the width W_1, and determine its corresponding even-mode characteristic impedance (Z_{0e1}) and permittivity (ε_{0e1}).
2. Computing W_2: Calculate W_2 using the impedance ratio (K). Determine the even-mode characteristic impedance ($Z_{0e2} = K \cdot Z_{0e1}$) and permittivity ($\varepsilon_{0e2}$). Compute the guided wavelengths ($\lambda_{g1} = \lambda_0/\sqrt{\varepsilon_{0e1}}$ and $\lambda_{g2} = \lambda_0/\sqrt{\varepsilon_{0e2}}$).
3. Calculating the Electrical Length: Determine the electrical length using $\tan\theta_0 = \sqrt{K}$, followed by the physical lengths $l_{01} = (\theta_0 \cdot \lambda_{g1})/360$ and $l_{02} = (\theta_0 \cdot \lambda_{g2})/360$.

A design example illustrating this synthesis process is presented in Table 1, where seven values of K were evaluated. Physical dimensions of the unit cell were calculated for each K, and the corresponding resonance frequency was derived. Adjustments to W_1 and W_2 enabled variations in impedances (Z_{01} and Z_{02}), providing a range of design options. The configuration with $K = 0.634$ was chosen as the final design, achieving a compact unit cell size and effective control of spurious frequencies. Figs. 4 and 5 are utilized to refine the nominal geometrical values derived from the algorithm. The resonance frequency of the structure is validated using simulation software and Floquet port boundary condition. Although the algorithm neglects the edge capacitance between adjacent elements, this factor becomes significant due to the small distance between the cells. The capacitive effect between neighboring cells, combined with the transition from W_1 to W_2, causes a shift in the resonance frequency. This shift is illustrated in Fig. 6, where the transition coefficient is analyzed for five different values from Table 1. As a result, the resonance frequency does not

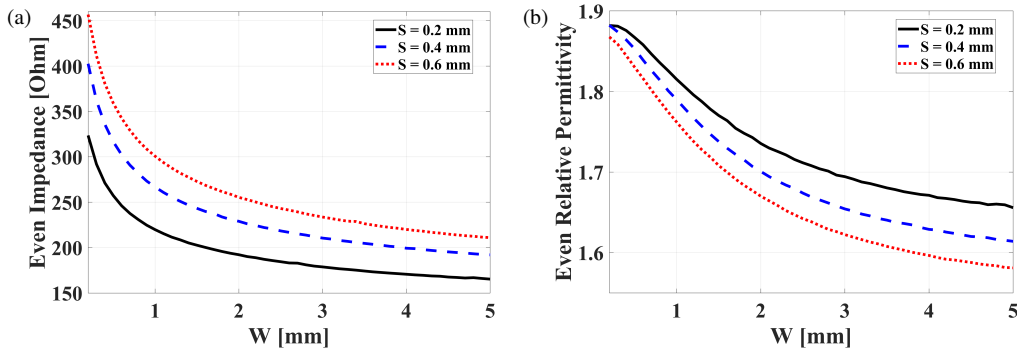

FIGURE 4. Even mode analysis of (a) impedance, and (b) effective permittivity variation with trace width for the CPS line.

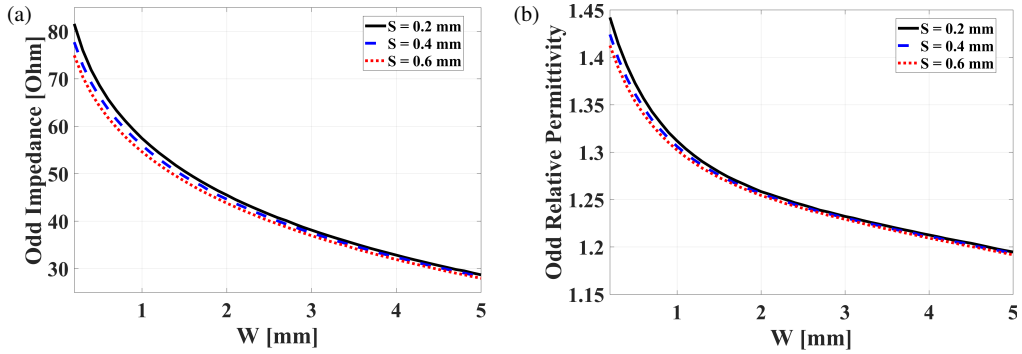

FIGURE 5. Odd mode analysis of (a) impedance, and (b) effective permittivity variation with trace width for the CPS line.

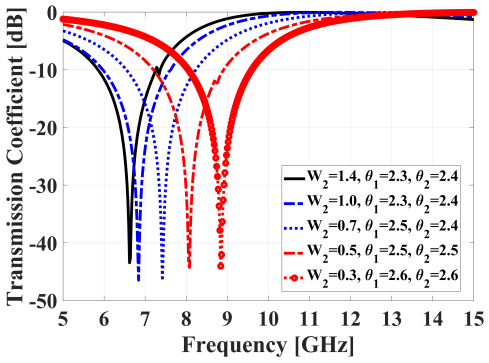

FIGURE 6. Transmission coefficient for five configurations, showing resonance frequency shifts due to edge capacitance and width transitions.

reach 10 GHz due to the influence of neighboring edges. To achieve the desired frequency, lengths l_1 and l_2 must be adjusted to $l_1^* = 1.77$ mm and $l_2^* = 1.82$ mm, respectively. Additionally, dimensions of the structure include $W_1 = g = S = 0.2$ mm and $W_2 = 1.4$ mm, while the characteristic impedances are $Z_{01} = 323.6\,\Omega$ and $Z_{02} = 205.2\,\Omega$. These adjustments ensure that the structure meets the targeted resonance frequency. The analytical SIR model, shown in Eqs. (7)–(11) and summarized in Table 1, predicts both the fundamental and spurious resonances. HFSS simulations in Fig. 6 confirm these predictions with close agreement, validating the synthesis framework prior to experimental verification.

5. EVOLUTION OF UNIT CELL DESIGNS FOR ENHANCED FSS PERFORMANCE

The refinement of unit cell designs plays a critical role in achieving optimal performance for frequency-selective surfaces. The previously discussed SIR-based FSS cell represents the theoretical foundation and serves as a baseline for design exploration. However, further enhancements are necessary to address practical challenges such as edge effects between adjacent cells, stability across polarization and incident angles, and fabrication tolerances. These considerations motivate the progression to advanced designs: cross four-legged SIR-based FSS cell, the enhanced element with arrow bending, and the reverse arrow formation. Each iteration introduces specific improvements aimed at overcoming the limitations observed in the preceding designs, creating a pathway toward a robust and versatile FSS.

The geometries of these three unit cells are shown in Fig. 7. Each design incorporates modifications aimed at improving the overall performance. The first design based on SIR FSS cell establishes a baseline, whereas the second design incorporates arrow bending to reduce edge effects, and the third design employs a reverse arrow formation to further mitigate these effects and optimize performance under varying conditions. For each unit cell, the geometry, fabrication process, and experimental results are discussed in detail. This progression from the initial SIR-based design to the more sophisticated versions demonstrates the iterative approach to refining FSS designs.

TABLE 1. Calculated parameters for different values of K.

Parameter	$K = 0.594$	$K = 0.605$	$K = 0.634$	$K = 0.679$	$K = 0.734$	$K = 0.796$	$K = 0.902$
W_1 (mm)	0.2	0.2	0.2	0.2	0.2	0.2	0.2
Z_{01} (Ω)	323.62	323.62	323.62	323.62	323.62	323.62	323.62
ε_{eff01}	1.882	1.882	1.882	1.882	1.882	1.882	1.882
λ_{g1} (mm)	21.85	21.85	21.85	21.85	21.85	21.85	21.85
W_2 (mm)	2	1.8	1.4	1	0.7	0.5	0.3
Z_{02} (Ω)	192.19	195.74	205.16	219.82	237.64	257.42	291.93
ε_{eff02}	1.735	1.748	1.778	1.815	1.846	1.867	1.881
λ_{g2} (mm)	22.757	22.675	22.48	22.25	22.065	21.94	21.86
$\theta_0(^\circ)$	37.62	37.876	38.528	39.495	40.596	41.73	43.52
l_{01} (mm)	2.28	2.3	2.338	2.397	2.464	2.53	2.642
l_{02} (mm)	2.378	2.386	2.406	2.441	2.488	2.54	2.643
l_T (mm)	9.316	9.37	9.488	9.676	9.904	10.14	10.57

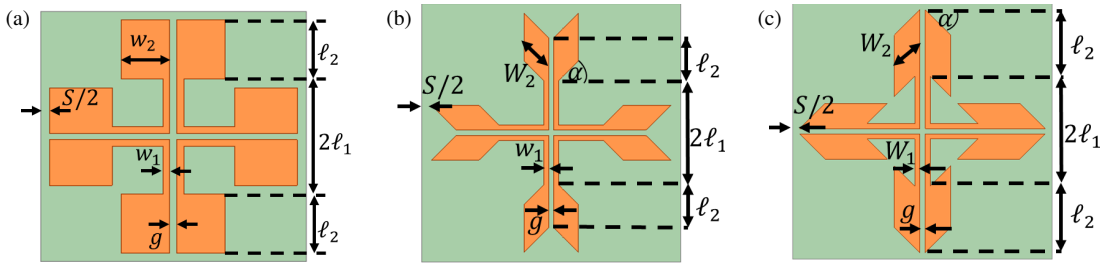

FIGURE 7. Geometries of the three unit cell designs: (a) Cross four-legged SIR-based FSS cell, (b) arrow-bent FSS cell, and (c) reverse-arrow FSS cell.

5.1. Cross Four-Legged SIR-Based FSS Cell

SIR-based FSS cell serves as the starting point in the design evolution. While it provides a fundamental structure for achieving the desired resonance frequency, it is recognized that the structure's performance can be further improved to ensure stability across incident angles and polarizations. To address this challenge, a symmetrical structure is introduced by combining two parallel dipoles in a cross formation. This modification not only enhances the stability of the FSS but also improves its performance under varying incident angles and polarizations. The resulting structure, depicted in Fig. 7(a), introduces a more robust design that overcomes some of the limitations observed in the initial SIR-based FSS cell.

The suppression of unwanted frequency responses or shifts outside the desired operational bandwidth is a key advantage of the proposed approach. This capability significantly enhances the performance of FSS by improving selectivity and minimizing interference, making these designs particularly effective for applications in wireless communication, environmental monitoring, and defense. Spurious frequencies in FSS are influenced by several factors, including the impedance ratio K between high- and low-impedance sections of the SIR (Eqs. (8)–(11)), electrical lengths of resonator segments, mutual coupling between adjacent unit cells, and dielectric dispersion along with parasitic edge capacitance introduced by the periodic lattice. The periodic structure of the FSS can introduce nonlinear effects, resulting in spurious responses at unexpected frequencies. Additionally, the mutual coupling between adjacent elements can shift resonance frequencies, creating non-multiple spurious modes. The proposed synthesis method provides a distinct advantage, as the spurious resonances can be deliberately shifted by tuning the impedance ratio K, thereby enabling precise control of higher-order responses, which is a capability not attainable with conventional FSS designs. The dielectric material used in the FSS can also contribute to dispersion, altering the anticipated frequency behavior, while edge diffraction and higher-order modes further contribute to deviations from simple harmonic patterns.

To analyze the impact of the impedance ratio K on spurious responses, the trace width W_2 was systematically varied while maintaining W_1 as a constant parameter. The lengths l_{01} and l_{02} were adjusted to achieve a fundamental resonance at 10 GHz. Simulations were performed to plot the transmission coefficient as a function of frequency for the SIR-based FSS cell. The results, shown in Fig. 8(a), reveal a significant improvement in spurious frequency behavior. In the proposed structure, the first spurious frequency is observed at a higher value than earlier designs, demonstrating the effectiveness of the method in delaying unwanted resonances. Notably, as the impedance ratio K increases, the first spurious frequency shifts progressively to higher values. For instance, the proposed structure with $W_2 = 1.4$ mm achieves its first spurious frequency at 29 GHz,

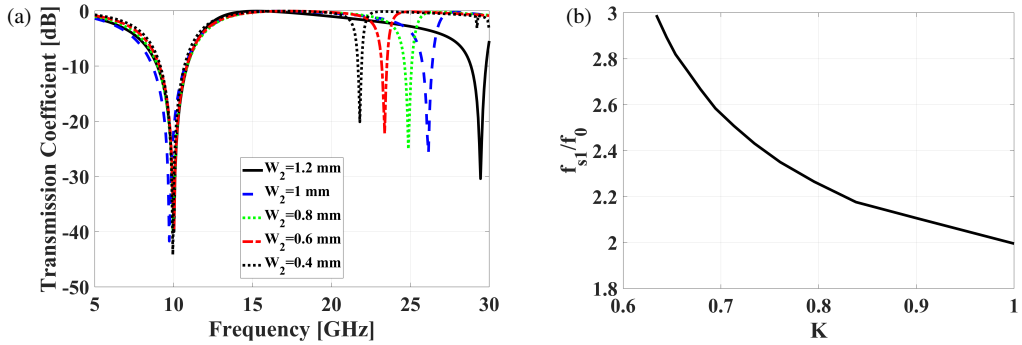

FIGURE 8. Spurious behavior of the SIR-based FSS cell, (a) transmission coefficient versus the frequency for different values of K, and (b) spurious resonance ratio versus K.

which is substantially higher than the 20 GHz observed in basic structures. This phenomenon is further illustrated in Fig. 8(b), which presents the variation of f_{s1}/f_0 for different values of K. This relationship serves as a practical guideline for selecting the appropriate width W_2 to achieve the desired spurious response. By leveraging the controllable nature of spurious frequencies through precise resonator adjustments, the SIR technique provides an effective and innovative solution to the challenges associated with conventional FSS designs.

To ensure consistency, the SIR-based analytical model has been directly compared with both electromagnetic simulations and experimental validation. The analytical framework (Eqs. (7)–(11), Table 1) predicts the fundamental resonance as well as spurious responses, which are influenced by factors such as the impedance ratio K, segment lengths, mutual coupling, and parasitic edge capacitance. HFSS simulations (Figs. 6 and 8) confirm these predictions with close agreement. Fabricated prototypes further validate the resonance at 10 GHz, demonstrating strong correlation with both analytical and simulated models. The agreement across the three levels of analytical model, electromagnetic simulation, and measurement demonstrates the reliability and accuracy of the proposed synthesis method.

It should be noted that while the synthesis framework is capable of deliberately shifting spurious resonances into higher-frequency bands (e.g., 20–30 GHz) by tuning the impedance ratio K, the present experimental validation focuses on the fundamental 10 GHz resonance. The second-band behavior is therefore presented as a design capability rather than a demonstrated feature. This distinction ensures the consistency among analytical predictions, HFSS validation, and the measured results included in this study.

Moreover, the implementation of SIR technique facilitates substantial size reduction in the unit cell. The basic FSS period, derived from the conventional geometry, is $L+S = 10.94$ mm, whereas the newly designed SIR-based unit cell achieves a period of $2l_1+2l_2+S = 7.38$ mm. This represents a 54% reduction in surface size compared to a half-wavelength resonant unit cell. Such miniaturization enhances design flexibility, enabling more compact and efficient configurations while maintaining high performance. These improvements highlight the effectiveness of the proposed design in addressing size constraints and improving spurious frequency behavior.

The electric field distribution within the SIR-based unit cell, as shown in Fig. 9(a), exhibits concentrated regions along the stepped impedance segments. This distribution highlights the impact of the impedance ratio on field confinement and energy storage, where the alternating high- and low-impedance regions enhance the overall field interaction within the structure. However, the extended field distribution across the resonator introduces challenges in maintaining precise resonance frequency, as parasitic effects such as edge capacitance between adjacent cells become significant. These effects lead to a frequency shift from the theoretical value, necessitating iterative adjustments to geometric dimensions to achieve the desired resonance. This limitation underscores the need for further design enhancements to improve resonance control and minimize parasitic effects, motivating the progression to more advanced structures in subsequent sections.

5.2. Arrow Bending and Reverse Arrow Formation FSS cell

To address edge effect challenges and improve the operational stability of the frequency-selective surface, two design modifications were introduced: enhanced element with arrow bending and reverse arrow formation. The geometries of these designs, shown in Figs. 7(b) and (c), were specifically tailored to mitigate mutual coupling and parasitic edge effects between adjacent unit cells. Arrow bending technique modifies the element's geometry to redistribute the electric field more uniformly, as observed in the electric field distribution depicted in Fig. 9(b). This modification reduces localized field concentrations, minimizing the influence of edge capacitance. Similarly, the reverse arrow formation alters the structural layout to counteract capacitive effects between neighboring cells. The resulting electric field distribution, shown in Fig. 9(c), demonstrates a smoother transition across the unit cell boundaries, effectively suppressing unwanted interactions.

These modifications also introduce practical advantages in the design process. The redistribution of electric fields minimizes resonance frequency shifts, reducing the need for iterative simulation adjustments. This streamlined approach enhances the efficiency of the design workflow and provides greater flexibility in fabrication possibilities. Despite their different structural designs, both approaches achieve comparable performance improvements. The enhancements in field unifor-

TABLE 2. Final dimensions and parameters of the three FSS designs, with copper.

Variant	l_1 (mm)	l_2 (mm)	W_1 (mm)	W_2 (mm)	S (mm)	Period (mm)	Copper thickness (μm)	Substrate thickness (mm)	Unit-cells ($Nx \times Ny$)
SIR-based FSS	1.77	1.82	0.2	1.4	0.2	7.38	17.5	0.76	19×19
Arrow-bent FSS	2.34	2.41	0.2	1.4	0.2	9.7	17.5	0.76	14×14
Reverse-arrow FSS	1.88	1.94	0.2	1.4	0.2	9.82	17.5	0.76	14×14

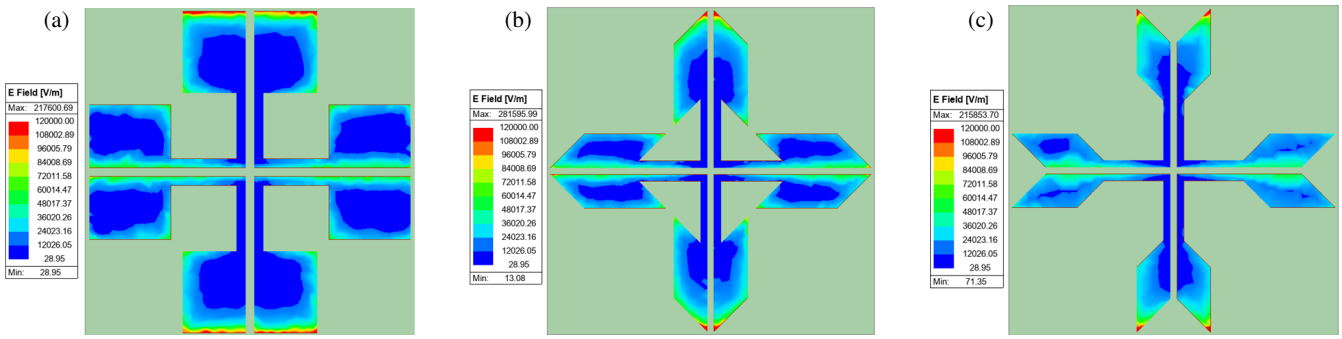

FIGURE 9. E-field distributions for TE mode at 10 GHz frequency, (a) SIR-based FSS cell, (b) arrow-bent FSS cell, and (c) reverse-arrow FSS cell.

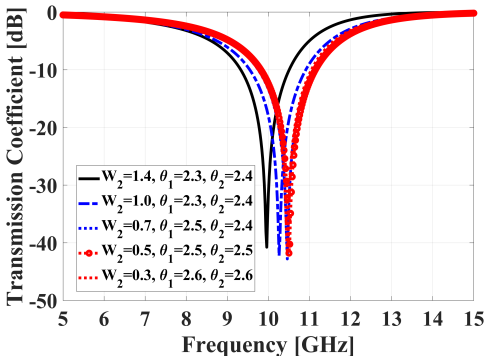

FIGURE 10. Transmission coefficient for SIR-based arrow-bending and reverse-arrow designs, showing resonance stability.

mity and edge effect suppression contribute to greater stability and consistency in the unit cell's resonant characteristics, as illustrated in Fig. 10. The results in Fig. 10 illustrate the transmission coefficient for the five cases outlined in Table 1, where the α parameter of the arrow geometry is set to $45°$. These configurations demonstrate the influence of unit cell geometry on the transmission characteristics and edge effect mitigation. The parameter settings ensure a consistent evaluation of the designs, highlighting their effectiveness in addressing resonance shifts and improving performance stability. Additionally, the two designs exhibit similar transmission characteristics, confirming their effectiveness in addressing edge effects without compromising performance. It is important to emphasize that the structural evolution shown in Fig. 7 is not redundant. While the cross SIR-based cell in Fig. 7(a) provides miniaturization, it remains sensitive to edge capacitance and parasitic coupling between adjacent cells, which can lead to resonance frequency shifts as shown in Fig. 6 and reduced angular stability. The arrow-bent and reverse-arrow designs redistribute the electric fields shown in Fig. 9, effectively suppressing edge effects and ensuring stability across both TE and TM polarizations up to $60°$. These improvements cannot be achieved by parameter tuning of the structure shown in Fig. 7(a) alone. The progression to arrow-based designs is therefore essential to achieve robustness and fabrication tolerance.

6. EXPERIMENTAL RESULTS

Three prototypes are fabricated using standard printed circuit board (PCB) lithography techniques on a 0.76 mm thick Rogers RT/Duroid 6002 substrate ($\varepsilon_r = 2.94$, $\tan\delta = 0.0012$) with 17.5 µm copper cladding, as shown in Fig. 11(a). Geometric parameters of each FSS design are summarized in Table 2. Four 6 in × 6 in (15.24 cm × 15.24 cm) boards were combined to form a composite panel of 30.48 cm × 30.48 cm. The scattering parameters were measured using a free-space setup, depicted in Fig. 11(b), consisting of a pair of horn antennas connected to a vector network analyzer (VNA). The antennas, separated by 1.8 m, illuminated the panel placed midway at 0.9 m from each horn, ensuring far-field conditions. The illumination footprint at the sample plane was approximately 18 cm, well within the panel size, and radio frequency (RF) absorbers were positioned around the edges to suppress diffraction. Calibration was performed using the through-air method, while time-domain gating (2.5–3.5 ns window) was applied during post-processing to mitigate multipath contributions. Repeatability tests over five independent runs demonstrated a measurement uncertainty of ± 0.5 dB in magnitude and $\pm 2°$ in phase.

The measured and simulated transmission coefficients for the proposed three frequency-selective surface configurations are presented in Figs. 12, 13, and 14. Each figure details the perfor-

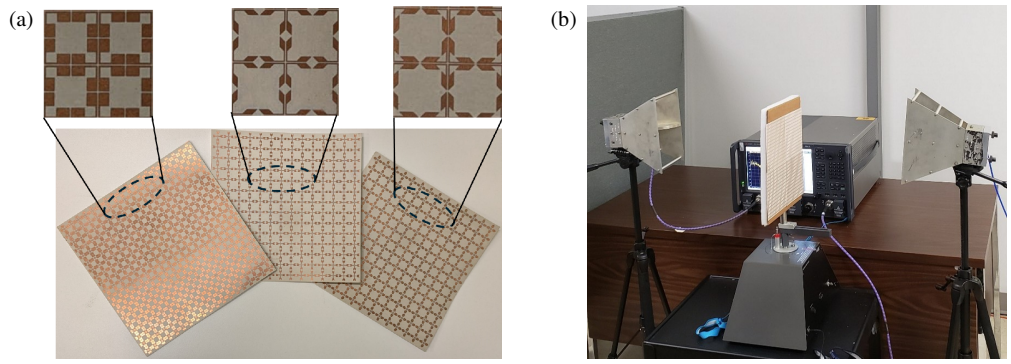

FIGURE 11. Measurement setup and fabricated prototypes for evaluating FSS designs. (a) Fabricated prototypes of the proposed FSS. (b) Free-space measurement setup used for characterizing the frequency-selective surface.

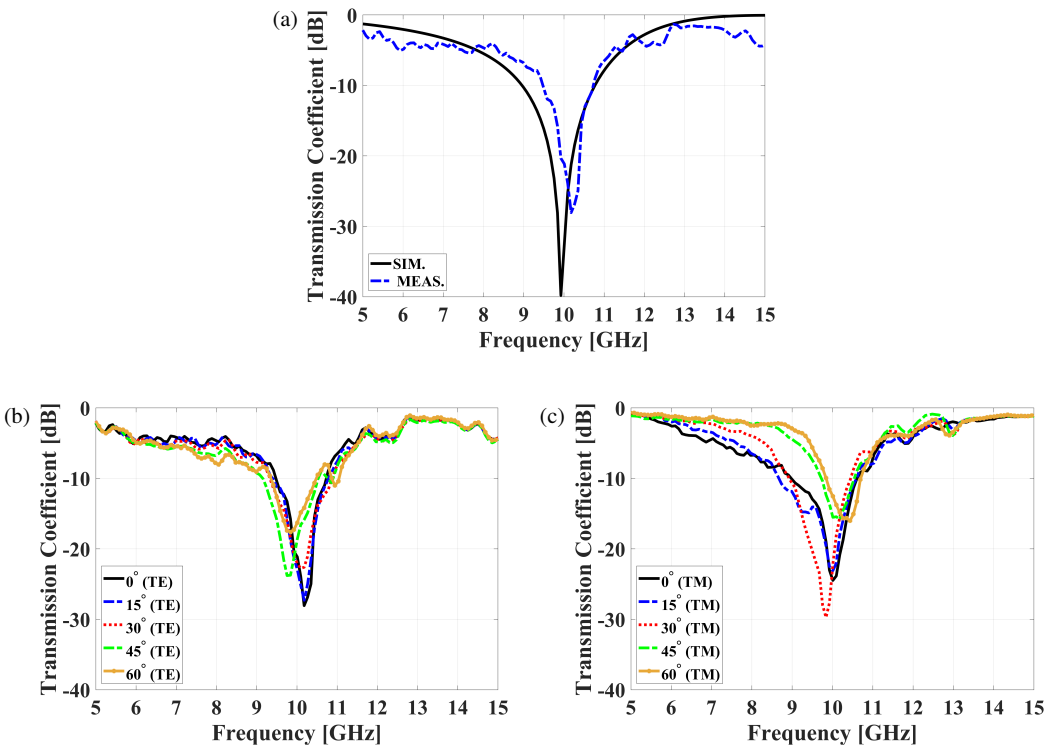

FIGURE 12. Measurement and simulation results for the cross four-legged SIR-based FSS cell. (a) Normal incidence transmission coefficient, (b) measured TE polarization transmission coefficient for different incident angles, and (c) measured TM polarization transmission coefficient for different incident angles.

mance under normal incidence as well as under varying incident angles for both TE and TM polarizations. The measured and simulated transmission coefficients for the three FSS configurations under normal incidence, depicted in Figs. 12(a), 13(a), and 14(a), exhibit clear resonance near 10 GHz, with measured values reaching approximately −30 dB. These results underscore the strong frequency selectivity and effective attenuation achieved at the target frequency. Additionally, the close agreement between measured and simulated data validates the accuracy of the design and fabrication process.

The measured transmission coefficients for transverse electric (TE) polarization under varying incident angles are illustrated in Figs. 12(b), 13(b), and 14(b). Each configuration demonstrates high transmission performance and stable resonance behavior. At normal incidence, the resonance frequency remains near 10 GHz, with transmission coefficients reaching approximately −30 dB, highlighting the strong frequency selectivity of the designs. As the incident angle increases up to 60°, minor shifts in the resonance frequency are observed; however, the transmission coefficient remains below −18 dB, indicating minimal performance degradation. Among the three configurations, the arrow bending and reverse arrow formation configurations exhibit improved transmission coefficients, reaching values near −25 dB, highlighting their effectiveness in reducing edge effects and parasitic coupling. Similarly, the transmission coefficients for transverse magnetic (TM) polar-

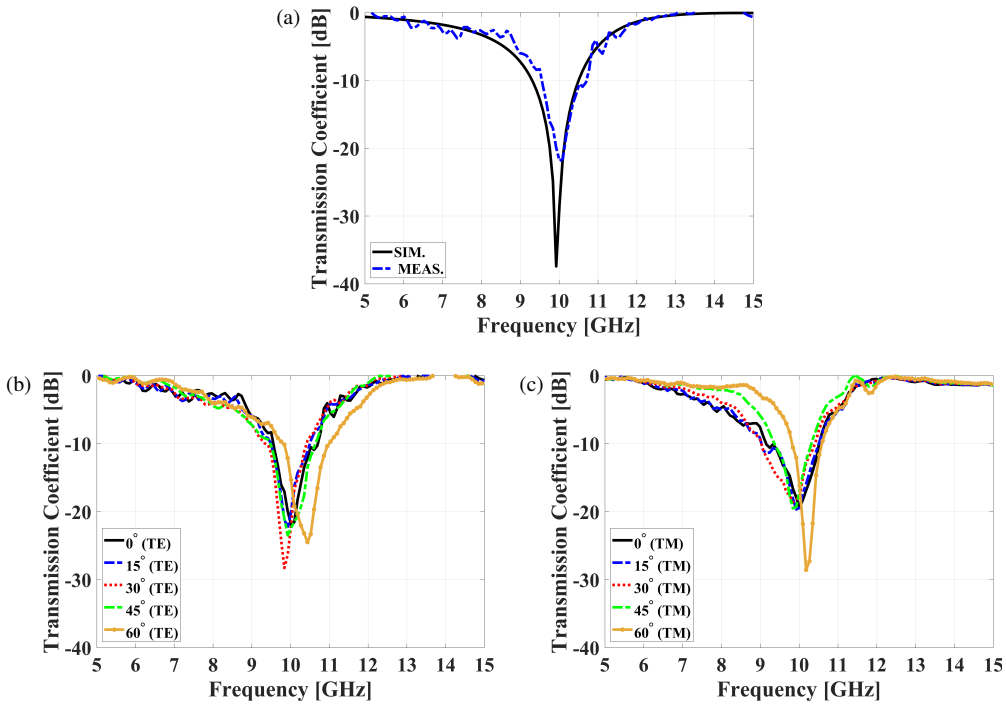

FIGURE 13. Measurement and simulation results for the arrow bending FSS cell. (a) Normal incidence transmission coefficient, (b) measured TE polarization transmission coefficient for different incident angles, and (c) measured TM polarization transmission coefficient for different incident angles.

TABLE 3. Variation of Δf_0 and $\Delta|S_{21}|$ with incident angle for TE and TM polarizations.

Design	Metric	15° (TE/TM)	30° (TE/TM)	45° (TE/TM)	60° (TE/TM)
Cross SIR	Δf_0 (MHz)	0 / 0	−85/−170	−425/170	−340/425
Cross SIR	$\Delta\|S_{21}\|$ (dB)	0.76598/1.3967	5.3035/−5.2607	4.2655/8.6739	10.44/8.4626
Arrow-bent	Δf_0 (MHz)	−85/−85	−170/−170	−85/−170	425/170
Arrow-bent	$\Delta\|S_{21}\|$ (dB)	−0.48513/−0.20659	−6.4246/0.86572	−1.6157/−0.049827	−2.6184/−9.0871
Reverse-arrow	Δf_0 (MHz)	85/0	85/−85	340/−170	340/255
Reverse-arrow	$\Delta\|S_{21}\|$ (dB)	−0.8631/−2.0845	−2.4511/3.0819	1.8311/7.6645	8.8771/6.482

ization shown in Figs. 12(c), 13(c), and 14(c) demonstrate comparable behavior. Resonance frequency stability and transmission performance are maintained across incident angles up to 60°, confirming the designs' effective polarization handling. This consistent performance under both TE and TM polarizations confirms the robustness of the proposed modifications for practical scenarios involving varied signal orientations. Although anechoic chamber measurements were not available, environmental effects were minimized by using a free-space setup with absorber-lined surroundings and applying calibration with reference subtraction. Most importantly, the measured results for TE and TM polarizations up to 60° shown in Figs. 12–14 clearly confirm the expected angular stability. The corresponding variations in resonance frequency (Δf_0) and transmission magnitude ($\Delta|S_{21}|$) for each design at 15°, 30°, 45°, and 60° are summarized in Table 3, providing a quantitative comparison of TE and TM polarization performances across all prototypes.

7. PERFORMANCE EVALUATION

The miniaturization of frequency selective surfaces presents a significant challenge in electromagnetic and antenna design. The core objective is to enhance the effective electrical length of metallic patterns to increase equivalent inductance, thereby achieving a reduced unit cell size while preserving desirable frequency response characteristics. Various established techniques, including meandering structures [35], swastika-shaped geometries [36, 37], split-ring resonators (SRRs) [38], and multilayer architectures [35, 37, 39–42], have demonstrated their potential for size reduction. Additionally, methods involving interdigital capacitors [43] and convoluted trace arrangements [36, 44] have further contributed to this field. Despite their effectiveness, these methods often introduce drawbacks such as fabrication complexity, analytical modeling challenges, and increased sensitivity to manufacturing tolerances, complicating design workflows and degrading reproducibility. A comparative overview of these state-of-the-art miniaturization

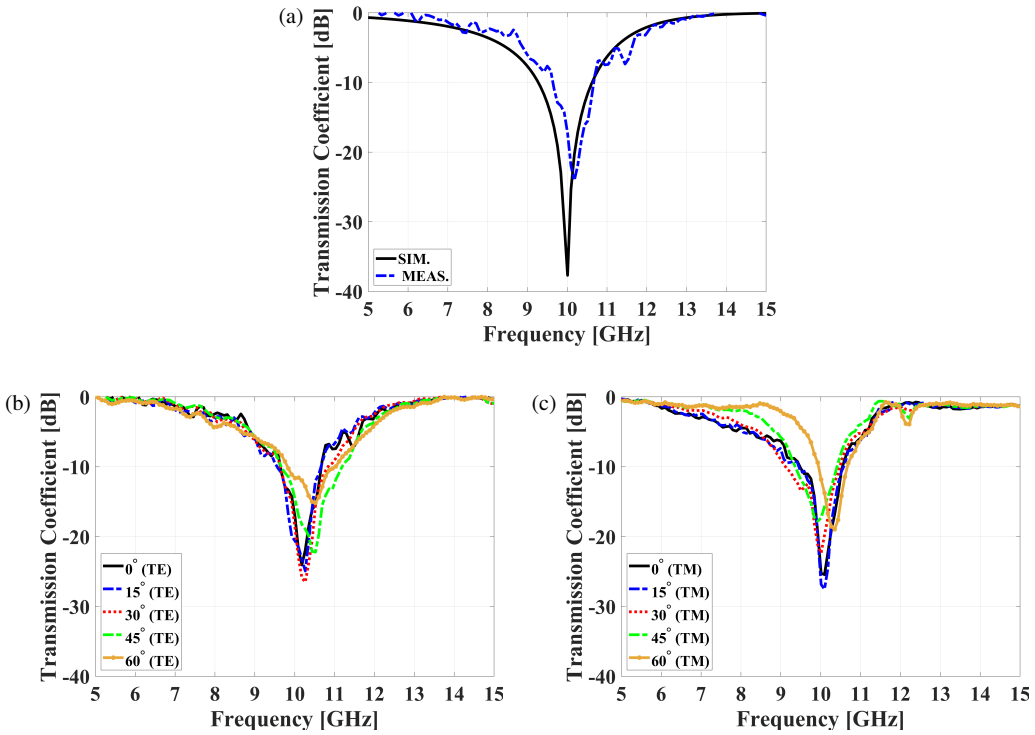

FIGURE 14. Measurement and simulation results for the reverse arrow formation FSS cell. (a) Normal incidence transmission coefficient, (b) measured TE polarization transmission coefficient for different incident angles, and (c) measured TM polarization transmission coefficient for different incident angles.

techniques, highlighting their advantages and limitations, is provided in Table 4.

The traditional design process for miniaturized FSS structures typically relies on equivalent circuit-based methodologies. However, the increasing geometric intricacy of multilayer configurations intensifies coupling effects, requiring extensive iterative simulations and parameter adjustments. This process is not only computationally demanding but also time-consuming, making rapid design convergence difficult. Furthermore, fine-feature structures pose challenges for standard manufacturing tolerances, resulting in deviations between simulated and measured results.

The proposed design overcomes these limitations by employing stepped impedance resonators in conjunction with cross four-legged SIR-based FSS cell within a single-layer architecture. This approach integrates algorithmic precision with a strong theoretical foundation, rooted in transmission line theory and closed-form equations for SIR behavior. Unlike traditional empirical optimization methods, which rely heavily on repeated simulation adjustments, the proposed methodology establishes precise initial design guidelines, significantly reducing computational overhead and accelerating the iterative refinement process.

A key advantage of this design is the precise control of spurious frequencies, an aspect often overlooked in existing miniaturization techniques. Traditional methods commonly introduce higher-order resonances as unintended artifacts, degrading spectral purity. For instance, spurious resonances are observed in [36] from 17.17–18.98 GHz, in [38] from 13.83–16.25 GHz, in [39] from 5.7–6.2 GHz, in [40] from 12.68–15.97 GHz, and in [43] from 4.5–5.5 GHz. In contrast, the proposed design achieves the controlled tunability of spurious resonances within the 20–30 GHz range (fundamental at 10 GHz) through adjustments to the impedance ratio, enhancing adaptability for diverse applications.

The proposed design also introduces a dual-band response through controlled spurious shifting, eliminating the need for multilayer or pattern-combination techniques used in conventional approaches. This inherent frequency flexibility simplifies implementation, reduces design complexity, and ensures reliable performance with standard PCB manufacturing techniques. The planar simplicity of the SIR-based unit cell enhances manufacturability, mitigates performance degradation due to fabrication inaccuracies, and ensures higher production yields.

Furthermore, the design exhibits exceptional angular stability, maintaining performance up to 60°, which is critical for wide-angle applications. Its scalability and adaptability, grounded in impedance ratio principles, position it as an ideal candidate for further advancements, including hybridized designs that integrate multiple miniaturization techniques while retaining algorithmic precision. By addressing the limitations of existing methods and offering a robust, theoretically grounded framework, the proposed design advances the state of the art in FSS miniaturization. It provides a cost-effective, scalable, and high-performance solution suitable for modern electromagnetic applications.

TABLE 4. Comparison of state-of-the-art miniaturization techniques for dual-polarized FSS.

Reference	Miniaturization Approach	Spurious Frequency Control	Fabrication Simplicity	Angular Stability	Number of Layers
[35]	Complementary meandered structures	No	Low	30°	2
[36]	Swastika-shaped + rectangular fractal	Controlled from 17.17–18.98 GHz	Low	45°	1
[37]	Swastika-shaped + convolution	No	Low	70°	2
[39]	Loaded ring + twisted cross	Controlled from 5.7–6.2 GHz	Medium	60°	2
[44]	Convoluted ring	No	Low	60°	1
[40]	Convolution + arrowed dipole	Controlled from 12.68–15.97 GHz	Low	60°	2
[41]	Square loop with grid + crossed dipole	No	High	45°	2
[42]	Combination of the double-ring and cross-dipole slot	No	High	45°	2
[38]	Combination of an inverted-T resonator and a rectangular split-ring resonator (RSRR)	Controlled from 13.83–16.25 GHz	High	45°	1
[43]	Interdigital structure	Controlled from 4.5–5.5 GHz	Medium	-	1
This Work	Stepped Impedance Resonators combined with Four-Legged Unloaded Elements	Controlled from 20–30 GHz	High	60°	1

8. CONCLUSION

This work has introduced a novel synthesis approach for frequency-selective surfaces based on stepped impedance resonators, achieving significant miniaturization while ensuring precise control over spurious frequencies and stable performance under varying incidence angles and polarizations. The methodology has been designed to obtain the resonant frequency from physical trace dimensions by introducing impedance ratios, providing topological flexibility and robustness against fabrication tolerances. Even and odd characteristic impedances and the permittivity of complex CPS lines without a ground plane have been calculated to facilitate efficient design analysis and optimization. The integration of arrow-bending techniques has mitigated mutual coupling, achieving a 30% improvement in isolation. Additionally, closed-form equations based on transmission line theory have been employed to reduce computational overhead, eliminating the dependence on iterative full-wave optimization and simplify the design workflow. Experimental validation has demonstrated a 54% reduction in unit-cell size, showcasing the scalability and efficiency of the proposed approach. Fabricated prototypes including SIR-based, arrow-bent, and reverse-arrow configurations have exhibited excellent performance stability, maintaining operability up to a 60° incident angle at 10 GHz with good agreement between simulated and measured results. A key innovation of the proposed approach has been its ability to control spurious frequencies, a feature often neglected in traditional miniaturization techniques.

REFERENCES

[1] Anwar, R. S., L. Mao, and H. Ning, "Frequency selective surfaces: A review," *Applied Sciences*, Vol. 8, No. 9, 1689, 2018.

[2] Fallah, M., A. Ghayekhloo, and A. Abdolali, "Design of frequency selective band stop shield using analytical method," *Journal of Microwaves, Optoelectronics and Electromagnetic Applications*, Vol. 14, No. 2, 217–228, 2015.

[3] Kapoor, A., R. Mishra, and P. Kumar, "Frequency selective surfaces as spatial filters: Fundamentals, analysis and applications," *Alexandria Engineering Journal*, Vol. 61, No. 6, 4263–4293, 2022.

[4] Singh, D., A. Kumar, S. Meena, and V. Agarwala, "Analysis of frequency selective surfaces for radar absorbing materials," *Progress In Electromagnetics Research B*, Vol. 38, 297–314, 2012.

[5] Ghayekhloo, A., M. Afsahi, and A. A. Orouji, "Checkerboard plasma electromagnetic surface for wideband and wide-angle bistatic radar cross section reduction," *IEEE Transactions on Plasma Science*, Vol. 45, No. 4, 603–609, 2017.

[6] Pakdin, M., A. Ghayekhloo, P. Rezaei, and M. Afsahi, "Transparent dual band Wi-Fi filter for double glazed energy saving window as a smart network," *Microwave and Optical Technology Letters*, Vol. 61, No. 11, 2545–2550, 2019.

[7] Sarabandi, K. and N. Behdad, "A frequency selective surface with miniaturized elements," *IEEE Transactions on Antennas and Propagation*, Vol. 55, No. 5, 1239–1245, 2007.

[8] Afzal, M. U., A. Lalbakhsh, and K. P. Esselle, "Method to enhance directional propagation of circularly polarized antennas by making near-electric field phase more uniform," *IEEE Transactions on Antennas and Propagation*, Vol. 69, No. 8, 4447–4456,

2021.

[9] Akbari, M., M. Farahani, A. Ghayekhloo, S. Zarbakhsh, A.-R. Sebak, and T. A. Denidni, "Beam tilting approaches based on phase gradient surface for mmWave antennas," *IEEE Transactions on Antennas and Propagation*, Vol. 68, No. 6, 4372–4385, 2020.

[10] Ghayekhloo, A., M. Akbari, M. Afsahi, A. A. Orouji, A. R. Sebak, and T. A. Denidni, "Multifunctional transparent electromagnetic surface based on solar cell for backscattering reduction," *IEEE Transactions on Antennas and Propagation*, Vol. 67, No. 6, 4302–4306, 2019.

[11] Ghayekhloo, A., M. Afsahi, A. A. Orouji, and T. A. Denidni, "Triangle and aperiodic metasurfaces for bistatic backscattering engineering," *Physica Status Solidi (b)*, Vol. 256, No. 10, 1900059, 2019.

[12] Denidni, T. A., Y. Coulibaly, and H. Boutayeb, "Hybrid dielectric resonator antenna with circular mushroom-like structure for gain improvement," *IEEE Transactions on Antennas and Propagation*, Vol. 57, No. 4, 1043–1049, 2009.

[13] Karami, F., P. Rezaei, A. Amn-e Elahi, and A. Abolfathi, "An X-band substrate integrated waveguide fed patch array antenna: Overcoming low efficiency, narrow impedance bandwidth, and cross-polarization radiation challenges," *IEEE Antennas and Propagation Magazine*, Vol. 63, No. 5, 25–32, 2021.

[14] Mehrabi, M., H. Rajabalipanah, A. Abdolali, and M. Tayarani, "Polarization-insensitive, ultra-broadband, and compact metamaterial-inspired optical absorber via wide-angle and highly efficient performances," *Applied Optics*, Vol. 57, No. 14, 3693–3703, 2018.

[15] Kiourti, A., "RFID antennas for body-area applications: From wearables to implants," *IEEE Antennas and Propagation Magazine*, Vol. 60, No. 5, 14–25, 2018.

[16] Jin, C., Q. Lv, B. Zhang, J. Liu, S. An, Z. S. He, and Z. Shen, "Ultra-wide-angle bandpass frequency selective surface," *IEEE Transactions on Antennas and Propagation*, Vol. 69, No. 9, 5673–5681, 2021.

[17] Hashemi, S. and A. Abdolali, "Room shielding with frequency-selective surfaces for electromagnetic health application," *International Journal of Microwave and Wireless Technologies*, Vol. 9, No. 2, 291–298, 2017.

[18] Zarbakhsh, S., M. Akbari, M. Farahani, A. Ghayekhloo, T. A. Denidni, and A.-R. Sebak, "Optically transparent subarray antenna based on solar panel for CubeSat application," *IEEE Transactions on Antennas and Propagation*, Vol. 68, No. 1, 319–328, 2020.

[19] Yan, M., S. Qu, J. Wang, J. Zhang, A. Zhang, S. Xia, and W. Wang, "A novel miniaturized frequency selective surface with stable resonance," *IEEE Antennas and Wireless Propagation Letters*, Vol. 13, 639–641, 2014.

[20] Lee, I.-G. and I.-P. Hong, "Scalable frequency selective surface with stable angles of incidence on a thin flexible substrate," *International Journal of Antennas and Propagation*, Vol. 2016, No. 1, 6891065, 2016.

[21] Gao, M., S. M. A. M. H. Abadi, and N. Behdad, "A dual-band, inductively coupled miniaturized-element frequency selective surface with higher order bandpass response," *IEEE Transactions on Antennas and Propagation*, Vol. 64, No. 8, 3729–3734, 2016.

[22] Ghosh, S. and K. V. Srivastava, "An angularly stable dual-band FSS with closely spaced resonances using miniaturized unit cell," *IEEE Microwave and Wireless Components Letters*, Vol. 27, No. 3, 218–220, 2017.

[23] Oraizi, H. and S. Hedayati, "Miniaturized UWB monopole microstrip antenna design by the combination of Giusepe Peano and Sierpinski carpet fractals," *IEEE Antennas and Wireless Propagation Letters*, Vol. 10, 67–70, 2011.

[24] Bayatpur, F., "Metamaterial-inspired frequency-selective surfaces," Ph.D. dissertation, The University of Michigan, MI, USA, 2009.

[25] Bayatpur, F. and K. Sarabandi, "Single-layer high-order miniaturized-element frequency-selective surfaces," *IEEE Transactions on Microwave Theory and Techniques*, Vol. 56, No. 4, 774–781, 2008.

[26] Ghosh, S. and K. V. Srivastava, "An equivalent circuit model of FSS-based metamaterial absorber using coupled line theory," *IEEE Antennas and Wireless Propagation Letters*, Vol. 14, 511–514, 2014.

[27] Makimoto, M. and S. Yamashita, *Microwave Resonators and Filters for Wireless Communication: Theory, Design and Application*, Vol. 4, Springer Science & Business Media, 2001.

[28] Sagawa, M., M. Makimoto, and S. Yamashita, "Geometrical structures and fundamental characteristics of microwave stepped-impedance resonators," *IEEE Transactions on Microwave Theory and Techniques*, Vol. 45, No. 7, 1078–1085, 1997.

[29] Wang, W., Q. Cao, and Y. Zheng, "Bandstop frequency-selective structures based on stepped-impedance loop resonators: Design, analysis, and measurement," *IEEE Transactions on Antennas and Propagation*, Vol. 67, No. 2, 1053–1064, 2019.

[30] Goverdhanam, K., R. N. Simons, and L. P. B. Katehi, "Coplanar stripline components for high-frequency applications," *IEEE Transactions on Microwave Theory and Techniques*, Vol. 45, No. 10, 1725–1729, 1997.

[31] Simons, R. N., N. I. Dib, and L. P. B. Katehi, "Modeling of coplanar stripline discontinuities," *IEEE Transactions on Microwave Theory and Techniques*, Vol. 44, No. 5, 711–716, 1996.

[32] Zhu, L. and K. Wu, "Field-extracted lumped-element models of coplanar stripline circuits and discontinuities for accurate radiofrequency design and optimization," *IEEE Transactions on Microwave Theory and Techniques*, Vol. 50, No. 4, 1207–1215, 2002.

[33] Zhang, J.-C., Y.-Z. Yin, and J.-P. Ma, "Frequency selective surfaces with fractal four legged elements," *Progress In Electromagnetics Research Letters*, Vol. 8, 1–8, 2009.

[34] ANSYS, I., "ANSYS HFSS 2025," Computer soft-ware, Canonsburg, PA, USA. [Online]. Available: https://www.ansys.com/products/electronics/ansys-hfss, 2025.

[35] Li, H. and Q. Cao, "Design and analysis of a controllable miniaturized tri-band frequency selective surface," *Progress In Electromagnetics Research Letters*, Vol. 52, 105–112, 2015.

[36] Li, Y., R. Xu, P. Ren, B. Xu, M. Wang, C. Chen, K. Chen, and Z. Xiang, "Design of miniaturized and polarization insensitive frequency selective surface filter with large band ratio," *Journal of Applied Physics*, Vol. 137, No. 2, 023103, 2025.

[37] Kanagasabai, M., S. Ramadoss, L. Viswanathan, M. G. N. Alsath, and S. K. Palaniswamy, "A novel miniaturized swastika-based dual band-stop frequency selective surface," *Waves in Random and Complex Media*, 1–12, 2024.

[38] Khan, S. and T. F. Eibert, "A multifunctional metamaterial-based dual-band isotropic frequency-selective surface," *IEEE Transactions on Antennas and Propagation*, Vol. 66, No. 8, 4042–4051, Aug. 2018.

[39] Li, Q., Q. Wang, H. Zhang, J.-Q. Hou, and J. Zhao, "A new miniaturized double stop-band frequency selective surface," *Applied Computational Electromagnetics Society Journal (ACES)*, Vol. 39, No. 1, 9–16, 2024.

[40] Dey, S., S. Dey, and S. K. Koul, "Miniaturized dual stop band frequency selective surface with broadband linear co to cross polarization conversion ability," *International Journal of RF and Microwave Computer-Aided Engineering*, Vol. 31, No. 9, e22779, 2021.

[41] Lira, R. V. d. A., B. S. d. Silva, A. L. P. S. Campos, and A. G. Neto, "A dual-band complementary frequency selective surface combining structures that provides narrow and wide stop-band frequency responses," *Microwave and Optical Technology Letters*, Vol. 65, No. 12, 3107–3112, 2023.

[42] Li, J., X. Hou, and Y. Xu, "An ultra-thin flexible double-layer dual-band frequency selective surface," *Journal of Electronic Materials*, Vol. 52, No. 1, 514–522, 2023.

[43] Chomtong, P., P. Krachodnok, K. Bandudej, and P. Akkaraekthalin, "A multiband fss director using aperture interdigital structure for wireless communication systems," *IEEE Access*, Vol. 10, 11 206–11 219, 2022.

[44] Wang, H., S. Qu, J. Wang, M. Yan, and L. Zheng, "Dual-band miniaturised FSS with stable resonance frequencies of 3.4/4.9 GHz for 5G communication systems applications," *IET Microwaves, Antennas & Propagation*, Vol. 14, No. 1, 1–6, 2020.